Thermal Sugar Bubbling Preparation of N-Doped Porous Carbon for High-Performance Solid-State Zn-Air Batteries

Si Chen,[a] Song Chen,[a] and Jintao Zhang*[a]

The rational design of metal-free carbon-based bifunctional electrocatalysts for lowering the energy barrier of oxygen reactions in metal-air batteries has a propelling effect on improving their overall performance. Herein, we reported the preparation of N-doped porous carbon materials with a large specific surface area of over 1900 $m^2 g^{-1}$ via thermal bubbling of glucose in the presence of cyanuric acid and ammonia chloride. When used as electrocatalysts, the porous carbon exhibited excellent bifunctional electrocatalytic activities for both, the oxygen reduction reaction (ORR) and the oxygen evolution reaction (OER). The potential gap ($\Delta E = E_{OER j = 10} - E_{ORR 1/2}$) between two reactions at the NPC-1000 catalyst is 0.72 V, which is even lower than that of the commercial electrocatalyst (e.g., Pt + RuO_2, ~0.80 V). The good bifunctional catalytic activities render the fabrication of high-performance rechargeable Zn-air batteries. Specifically, the flexible all-solid-state Zn-air battery assembled with NPC-1000 as the air cathode exhibited good charge-discharge stability and the voltage efficiency could be maintained about 58.6% even after cycling for 50 h. Furthermore, no obvious voltage decay was observed under various bending, showing the good mechanical flexibility.

1. Introduction

With the increasing fossil energy crisis and environmental pollution problems, efficient and sustainable clean energy conversion and storage technologies play an important role in addressing these problems.[1] Recently, metal-air batteries and fuel cells as important energy devices have received extensive attention.[2] Oxygen reduction reaction (ORR) and oxygen evolution reaction (OER) are two critical processes for metal-air batteries.[3] Therefore, the efficiency of these electrochemical reactions directly determines the ultimate performance of the energy devices. However, these electrochemical reactions need to overcome large overpotentials due to the high energy barriers.[4] Thus, high-efficiency electrocatalysts are the key to improve the conversion efficiency, selectivity and stability. Precious metal catalysts have excellent catalytic properties, for example, carbon-supported platinum catalysts (Pt/C)[5] exhibit good catalytic properties for ORR and hydrogen evolution reaction while noble metal oxides[6] (such as RuO_2, In_2O_3 etc.) exhibit high oxygen evolution catalytic performance. However, the high cost limits the widespread use of noble metal-based catalysts.[7] The development of non-precious metal catalysts with low cost, good stability and high activity is particularly important for reducing the energy barrier in the electrocatalytic reactions and accelerating the conversion rates.[8]
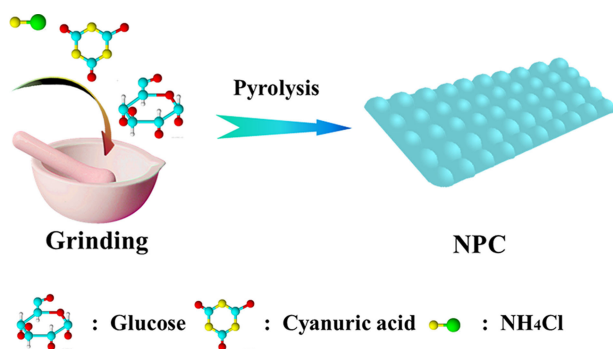
Heteroatom doped carbon materials have attracted extensive attention due to their good electrocatalytic activity and high stability.[9] The different electronic arrangements and electronegativity differences enable the changes of the electron distribution on the carbon surface in the presence of heteroatoms.[10] For example, the nitrogen-doped carbon nanotubes have a higher negative charge around the nitrogen atoms. Contrarily, the adjacent carbon atoms have a higher positive charge around them.[11] Therefore, the charge transfer caused by the electronegativity difference creates favorable active sites for the selective adsorption of O_2 molecules, which in turn improves the catalytic activities.[12] On the basis of the similar principles, Qu[13] et al. firstly synthesized the nitrogen-doped graphene for ORR via chemical vapor deposition, which showed good catalytic activity and stability. Recently, in order to explore the active sites of nitrogen-doped carbon materials, high-oriented pyrolytic graphite doped with different types of nitrogen as model catalysts. It is revealed that the catalytic activity is dependent on the content of pyridinic nitrogen.[14] However, it is still highly challenging to prepare nitrogen doped carbons as bifunctional electrocatalysts for both ORR and OER.

Herein, the porous N-doped graphitic carbon materials with large specific surface area were synthesized by in-situ gas generation for bubbling glucose due to the thermal decomposition of ammonia chloride and cyanuric acid (Scheme 1). The obtained carbon catalysts at an elevated temperature exhibited high-efficiency bifunctional catalytic activity for ORR and OER with a low potential difference of 0.72 V. More importantly, the rechargeable Zn-air batteries can be fabricated by using the as-prepared carbon electrocatalysts. Typically, the all-solid-sate Zn-air battery assembled with NPC-1000 catalyst as the air cathode exhibited good rate performance sand cycling stability under the bending states.

[a] S. Chen, S. Chen, Prof. J. Zhang
Key Laboratory for Colloid and Interface Chemistry
Ministry of Education
School of Chemistry and Chemical Engineering
Shandong University
Jinan, 250100, P.R. China
E-mail: jtzhang@sdu.edu.cn

Scheme 1. Preparation of nitrogen-doped porous carbon via the sugar bubbling process at an elevated temperature.

2. Results and Discussion

The nitrogen doped porous carbon (NPC) was synthesized by the carbonization of the mixture of glucose with cyanuric acid and NH_4Cl in an inert atmosphere. As demonstrated in Scheme 1, with the continuous increasing carbonization temperature, glucose would be gradually melted, resulting in the formation of liquid syrup. Along with the thermal decomposition of NH_4Cl, and cyanuric acid, the released gases would be used as the soft template to blow the syrup, leading to the generation of porous bubbles. Meanwhile, these nitrogen contained precursors also provide nitrogen sources for the formation of nitrogen doping.

The morphologies of NPC samples were characterized by using the scanning electron microscope (SEM) and transmission electron microscopy (TEM). The SEM images (Figure 1a and Figure S1) exhibit the porous carbon materials with abundant bubbles. The interconnected bubble-like structure is beneficial

to create abundant channels for the mass transfer of O_2 molecules and electrolyte.[15] TEM images (Figure S2 and Figure 1b) reveal the sheet-like structure of the bubbles wall, which would augment the specific surface area of NPC materials for exposing more active sites.[16] The enlarged TEM image (Figure 1d) exhibits the white spots, indicating the formation of highly porous structure. The graphitic carbon structure was demonstrated from the HRTEM image (Figure 1d). The lattice spacing of 0.34 nm is corresponding to the (002) spacing of graphitic carbon.[17] The elemental mapping images (Figure 1e) exhibit the uniform distribution of elements, C and N, suggesting the formation of nitrogen doped graphitic carbon.

The X-ray diffraction (XRD) patterns of NPC samples were performed to characterize the crystalline structure in Figure 2a.
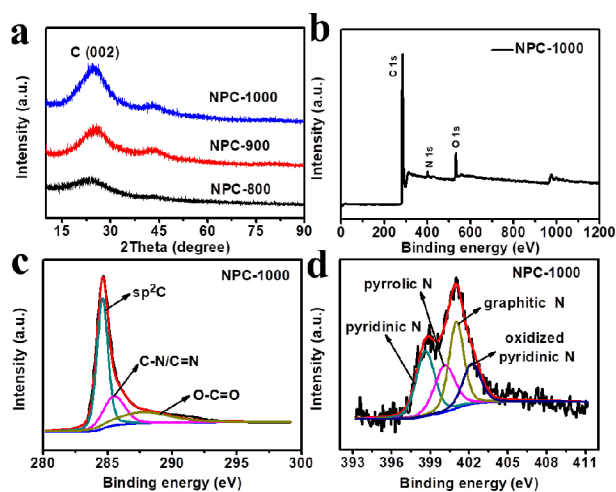

Figure 2. a) XRD patterns of NPC samples. b)-d) XPS Survey of NPC-1000 and high-resolution XPS spectra of C 1s, N 1s.

The peak at $\sim 24.5°$ is ascribed to the (002) facet of graphitic carbon. The increasing intensity suggests the enhanced graphitic degree with increasing pyrolysis temperature,[18] which would improve the electronic conductivity of carbon skeleton. X-ray photoelectron spectroscopy (XPS) was utilized to analyze the chemical composition of NPC samples.[19] The survey XPS of samples (Figure 2b and S3) exhibit the presence of carbon, nitrogen, and the adsorbed oxygen, which is in good agreement with the elemental mapping analysis. The core-level XPS spectra of C 1s in Figure 2c shows three bonds, corresponding to sp^2 C (284.6 eV), C=N/C—N (285.7 eV), O—C=O (287.4 eV), respectively.[20] As shown in Figure 2d, N 1s was deconvoluted into four parts according to pyridinic N (398.6 eV), pyrrollic N (400.8 eV), graphitic N (401.5 eV) and oxidized pyridinic N (404.0 eV). These results further confirm the thermally stable carbon matrix has been transferred into the nitrogen-doped graphitic carbon.[21] The nitrogen types for different samples were summarized in Figure S4. It can be seen that the ratio of pyrrollic nitrogen is gradually decreased with increasing the pyrolysis temperature. The pyridinic and graphitic N are the dominated type for the NPC-1000 sample. It has been revealed
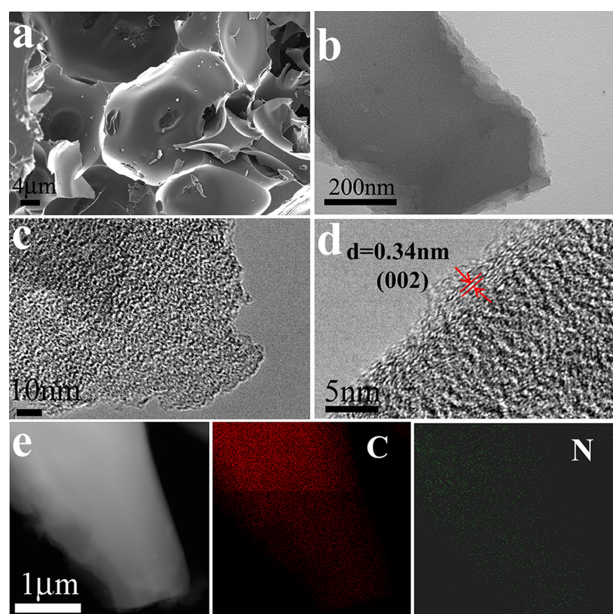

Figure 1. a) SEM image for NPC-1000. b)–c) TEM images for NPC-1000. d) HRTEM image for NPC-1000. e) The element mapping images for NPC-1000.

that the graphitic and pyridinic nitrogen would enhance the electrocatalytic activity for ORR.[22] Thus, the strong intensity and visible large area of pyridinic and pyrrollic nitrogen would generate more defect sites for efficient oxygen electrocatalysis.[23]

As shown in Figure 3a, Rama spectra exhibit that two obvious peaks at ~1350 and 1580 cm^{-1} are indexed to the D-
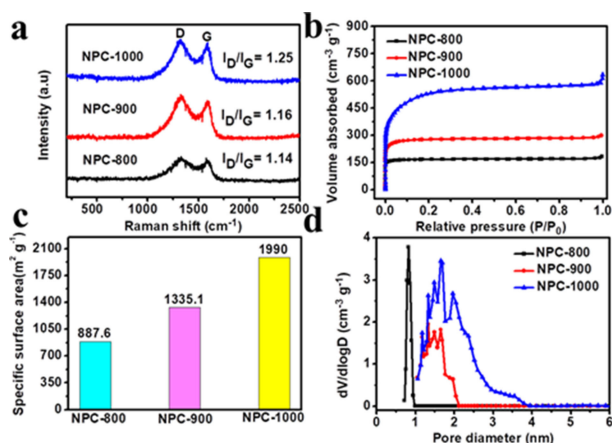

Figure 3. a) Rama spectrum of NPC samples. b) N_2 adsorption/desorption isotherm. c) Specific surface area. d) The pore size distribution curves.

and G- band, respectively.[24] The D-band presents the disordered sp^3 carbon whereas the G-band is assigned to the sp^2 graphitic carbon. With increasing pyrolysis temperature from 800 to 1000 °C, the increased intensity radio of I_D/I_G from 1.14 to 1.25 indicates the presence of abundant defects in the configuration, which would explore more active sites for the electrocatalysis.[25] The Brunauer-Emmett-Teller (BET) surface area and the pore size distribution were analyzed through N_2 adsorption/desorption isotherms.[26] Figure 3b shows the Type I isotherms with the largely increased volume below the relative pressure (P/P$_0$) of 0.1, revealing the existence of rich microporous structure.[27] The specific surface area (Figure 3c) was obtained about 887.6, 1335.1 and 1990 m^2 g^{-1} for NPC-800, NPC-900 and NPC-1000, respectively. The large specific surface area of samples is relational to the porous structure. The abundant micropores were further demonstrated through the pore size distribution curves in Figure 3d. From the pore size distribution plot, the small size about 1 nm for NPC-800 is observed. However, the pore sizes for NPC-900 and NPC-1000 gradually increase to mesoporous range centered at around 2 nm with increasing the pyrolysis temperature. The large surface area of NPC-1000 with highly porous structure would expose more active sites for improving the electrochemical reactions.[28]

As discussed above, the NPC samples exhibit highly porous structure with large surface area and nitrogen doping. It is expected to demonstrate enhanced electrocatalytic activities. To examine the electrochemical properties, the NPC catalysts were evaluated in 0.1 M KOH solution with/without the presence of oxygen. Cyclic voltammetry (CV) curves (Figure S5)

of NPC samples exhibit the obvious reduction peak in O_2-satuated KOH solution rather than N_2-satuated KOH solution is ascribed to the oxygen reduction. [29] Typically, NPC-1000 exhibits the highest onset potential at 0.99 V (vs. RHE) in comparison with NPC-800 (0.90 V vs. RHE) and NPC-900 (0.95 V vs. RHE), indicating the best electrochemical activity for ORR. The linear sweep voltammetry (LSV) plots were measured in O_2-satuated 0.1 M KOH solution with the rotating speed of 1600 rpm (Figure 4a). It is obviously observed that the NPC-900
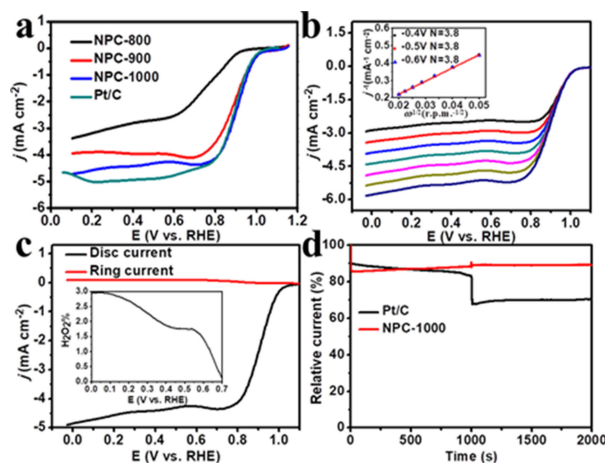

Figure 4. a) LSV curves of NPC-800, NPC-900, NPC-1000 and Pt/C in O_2-saturated 0.1 M KOH solution with the rotation speed of 1600 rpm. b) LSV curves of NPC-1000 at different rotation speed from 400 to 2500 rpm and the corresponding K–L plot (inset). c) RRDE measurement for NPC-1000 at the rotation speed of 1600 rpm and the percentage of peroxide (inset). d) Chronoamperometric response of NPC-1000 and Pt/C on addition of 1.5 M methanol with a rotation rate of 1600 rpm.

and NPC-1000 exhibit the similar onset potential, which is comparable to that of Pt/C, as a reference electrocatalyst. It can be seen that the NPC-1000 shows the best electrocatalytic activity in terms of the half-wave potential ($E_{1/2}$) of 0.91 V vs. RHE (0.80, 0.88 V and 0.91 V for NPC-800, NPC-900 and Pt/C, respectively) and the diffusion-limiting current density of around 5.0 mA cm^{-2}. The better performance of NPC-1000 electrocatalyst would be contributed to the large surface area with exposed active sites due to the porous structure.[30] LSV curves of NPC-1000 were measured at the rotation speed from 400 to 2500 rpm to determine the reaction kinetics of ORR (Figure 4b). The electron transfer number of NPC-1000 was calculated to be about 4.0 according to the Koutecky-Levich (K-L) equation (inset in Figure 4b), which represents the dominant four-electron pathway for oxygen reduction.[31]

The rotating ring disk electrode (RRDE) was utilized to collect the disk and ring current density at the rotation speed of 1600 rpm. As shown in Figure 4c, the ring current density is much lower in comparison with the large disk current density. The percentage of peroxide calculated is below 3.0%, further indicating the efficient four-electron reaction of oxygen reduction.[32] To evaluate the methanol tolerance of NPC-1000, 1.5 M methanol was added into the 0.1 M KOH electrolyte saturated with O_2 at the rotating speed of 1600 rpm. No obvious decay is

observed for NPC-1000, however in comparison with the rapid decline for Pt/C (Figure 4d). Therefore, the NPC-1000 exhibits excellent resistance to methanol cross-over effect, which is of importance for the potential application in direct methanol fuel cell.[33]

For the bifunctional applications, the electrocatalytic activity for OER is also tested. The OER catalytic activity was investigated by LSV curves on RDE in 0.1 M KOH electrolyte saturated with O_2 at 1600 rpm. As shown in Figure 5a, the
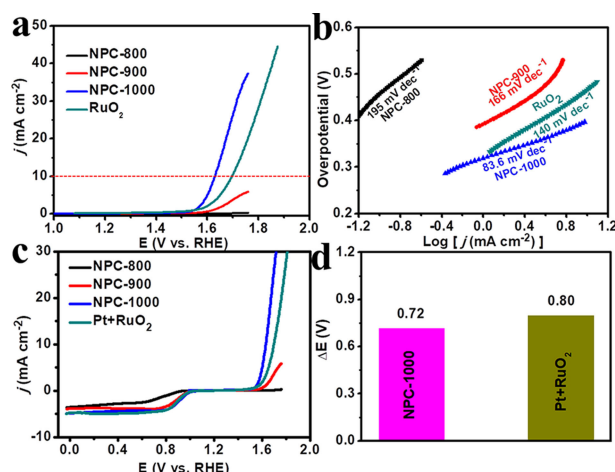

Figure 5. a) LSVs of NPC-800, NPC-900, NPC-1000 and RuO_2 for OER in 0.1 M KOH electrolyte saturated with O_2 at a rotating speed of 1600 rpm. b) The corresponding Tafel slopes. c) ORR and OER polarization plots of different samples. d) The value of ΔE for NPC-1000 and RuO_2 ($\Delta E = E_{j=10} - E_{1/2}$).

potential for OER to achieve a current density of 10 mA cm^{-2} is of 1.63 V vs. RHE at the NPC-1000 electrode, which is the lowest in comparison with NPC-800, NPC-900, and RuO_2 (1.71 V vs. RHE). The result indicates the best OER electrochemical activity of NPC-1000. The OER reaction kinetic was investigated via Tafel slopes obtained from the LSV polarization plots. NPC-1000 catalyst (Figure 5b) exhibits the minimum Tafel slope of 83.6 mV dec^{-1}, smallest than these of NPC-800 (195 mV dec^{-1}), NPC-900 (166 mV dec^{-1}), and RuO_2 (140 mV dec^{-1}), suggesting the favorable oxygen evolution reaction kinetics of NPC-1000. The electrochemical double-layer capacitance (C_{dl}) is commonly used to evaluate the electrochemical active area of a specific catalyst.[29b] According to the CV curves (Figure S7a–c) in 0.1 M KOH solution with the scan rates from 10 to 140 mV s^{-1}, the C_{dl} calculated of NPC-1000 (Figure S7d) is around 3.9 μF cm^{-2}, which is largest than these of NPC-800 (0.1 μF cm^{-2}) and NPC-900 (2.1 μF cm^{-2}). Thus, NPC-1000 has the largest electrochemical active area.[34] Additionally, electrochemical impedance spectroscopy (EIS) test (Figure S7e) exhibits that the smallest charge transfer resistance of NPC-1000 is around 13 Ω in comparison with NPC-800 (> 300 Ω) and NPC-900 (143 Ω). The NPC-1000 electrode with low charge transfer resistance would provide efficient charge transfer pathways, which would contribute to the better catalytic activity.

Generally, the potential difference between OER at the current density of 10 mA cm^{-2} and the half-wave potential of

ORR ($\Delta E = E_{j=10} - E_{1/2}$) is used to evaluate to the overall activity of bifunctional catalyst.[35] The lower potential gap portends the catalyst to be an ideal bifunctional electrocatalyst for oxygen electrocatalysis. As shown in Figure 5c, d, the potential gap of NPC-1000 is only 0.72 V, lower than that of the mixed $Pt + RuO_2$ catalyst (~ 0.80 V), indicating the better bifunctional catalytic activities of NPC-1000 catalyst for ORR and OER.

With the increasing demand on the portable electronic devices with high safety, solid-state batteries are attracted more and more attention as the promising energy sources. Thus, all-solid-state flexible Zn-air battery has been assembled by using the NPC catalysts as the air cathode. For comparison, $Pt + RuO_2$ mixed catalyst was also used to fabricate such batteries. Typically, the Zn-air battery with the NPC-1000 catalyst (Figure S8a) shows an open-circuit voltage of 1.45 V, which is even higher than that of Pt/C (1.39 V). Figure 6a shows the polar-
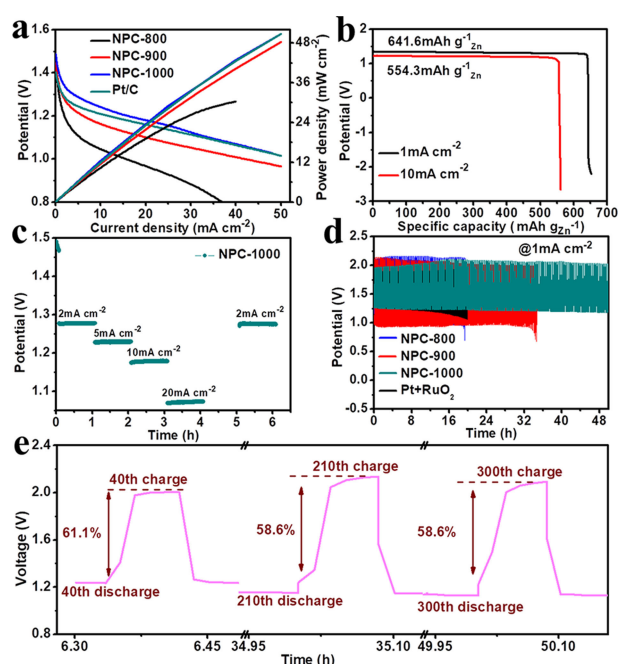

Figure 6. a) Polarization and power density curves of the rechargeable all-solid-state Zn–air battery. b) Galvanostatic discharge curves of Zn–air battery. The specific capacity is normalized by the mass of the consumed Zn. c) Galvanostatic discharge curves of Zn–air battery at different current density. d) Galvanostatic discharge–charge cycling curves of rechargeable Zn-air batteries assembled with different electrocatalysts. e) Voltage efficiency at the different charge-discharge cycles.

ization and power density curves for the all-solid-sate Zn-air batteries assembled with NPC and Pt/C catalysts. The peak power density for NPC-1000 is 50 mW cm^{-2}, which is superior to that of NPC-800 (30 mW cm^{-2}), NPC-900 (48 mW cm^{-2}) and even comparable to that of Pt/C (50 mW cm^{-2}). The large power density for NPC-1000 may be attributed to the porous structure with good catalytic activity for ORR. As shown in Figure 6b, the galvanostatic discharge curves of Zn-air battery assembled with NPC-1000 exhibit the voltage plateaus of 1.37 V and 1.21 V at the current density of 1 and 10 mA cm^{-2}, respectively. The specific capacities are 641.6 and 554.3 mAh g$_{zn}^{-1}$, correspond-

ing to the energy densities of 843.2 and 665.1 $Wh\,kg_{zn}^{-1}$, respectively when the discharge current density is 1 and 10 $mA\,cm^{-2}$. The decline of energy densities is attributed to the increase of polarization at the higher current density.[37] The rate performance is an important indicator to evaluate the quality of the Zn-air battery. Therefore, the galvanostatic discharge plots (Figure 6c) exhibit that the gradual changes on the discharge voltage of Zn-air battery assembled with NPC-1000 along with the increasing current density. The discharging potential could be retained at 1.08 V even at the current density up to 20 $mA\,cm^{-2}$. More importantly, the discharging voltage is around 1.27 V when the discharge current density is returned to 2 $mA\,cm^{-2}$. The results reveal that the solid-state Zn-air battery could discharge at higher current density, suggesting the good high-rate performance.[36] The negligible voltage decay for the NPC-1000 catalyst in comparison to Pt/C catalyst in the discharge process at 1 $mA\,cm^{-2}$ for 20 h indicates the good discharge stability (Figure S8b).

Figure S8c displayed the charge and discharge polarization curves for the Zn–air battery. We can see that the Zn-air battery using NPC-1000 electrocatalyst exhibits the lower charge potential and higher discharge platform than those using the Pt+RuO_2 at the same current density, which manifests the weak polarization in the discharge-charge process for NPC-1000. The efficiency and long-term cycling stability of NPC for all-solid-state Zn–air batteries was evaluated by the repeated galvanostatic charge discharge process. As demonstrated in Figure 6d, the Zn-air battery based on NPC-1000 catalyst provides a narrow charge-discharge potential gap of around 0.85 V, which is much lower than that of the noble-metal based reference. Notably, the battery can be repeatedly charged and discharged for 50 h, exhibiting the good cycling stability. As seen from the enlarged cycle profiles in Figure 6e, the Zn-air battery with the NPC-1000 air cathode shows slightly decay for the efficiency from 61.1% at the 40th cycle to 58.6% at the 210th cycle. After 300 cycles for 50 h, the battery could maintain the potential gap of around 0.85 V with the nearly unchanged efficiency of 58.6%. Especially, the NPC-1000 catalyst still performs excellent charge-discharge stability for 33 h when the current density is increase to be 5 $mA\,cm^{-2}$ (Figure S8d). The excellent performance of NPC-1000 benefits from the synergistic effect of the good bifunctional activities for both ORR and OER, thanks to the unique features of nitrogen doped carbon with highly porous structure and large specific surface area.[37]

The schematic illustration of the flexible all-solid-state Zn-air battery was showed in Figure 7a. Two batteries were connected to power LED in Figure 7b, demonstrating the promising applications. Figure 7c shows the mechanical flexibility test of the NPC-1000 based Zn-air battery at a current density of 1 $mA\,cm^{-2}$. The Zn-air battery was bended (180°) for each 10 cycles. Under the stable state of the battery, no obvious potential changes is observed when the battery is folded, suggesting the good flexibility of the solid-state Zn-air battery. The electrochemical impendence spectra of the all-solid-state Zn-air batteries (Figure S9) exhibit smaller charge transfer under the folded status. The enhanced contact between the air

electrode and the solid electrolyte would be enhanced, thus enhancing the charge transfer efficiency. The result suggests the good mechanical flexibility of the solid-state Zn-air battery. Additionally, in comparison with the reported results,[38–41] it can be seen that the Zn-air battery assembled with NPC-1000 catalyst exhibits the larger discharging potential and lower charging potential (Table S1). The stable cycling test for 50 h is much better than those of reported batteries, highlighting the good electrocatalytic stability of the as-prepared electrocatalyst.

3. Conclusions

In summary, a simple but efficient approach has been developed to synthesize nitrogen doped porous carbon via the thermal annealing of glucose in the presence of in the presence of cyanuric acid and ammonia chloride. The in-situ generation of gas due to the thermal decomposition of cyanuric acid and ammonia chloride resulted in the formation of porous carbon with large surface area. The electrochemical characterizations reveal the good bifunctional catalytic activities for oxygen reduction and oxygen evolution reactions, which enables the fabrication of high-performance rechargeable Zn-air battery. Typically, the flexible all-solid-state Zn-air battery assembled with NPC-1000 exhibited high power density of 50 $mW\,cm^{-2}$, good cycling stability for 50 hours, and great mechanical flexibility.

Experimental Section

Sample preparation: The composites were prepared by physical grinding the mixture of 0.2 g glucose, 0.2 g cyanuric acid and 1.2 g NH_4Cl. Then, the composites were transferred to the tube furnace and calcined at the temperature from 800 to 1000 °C in N_2
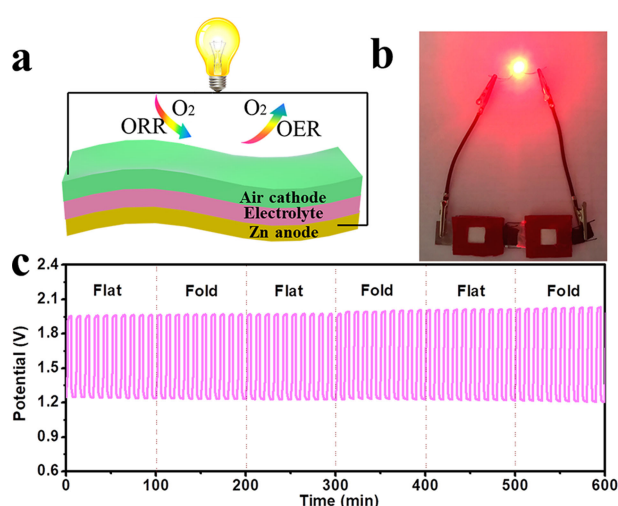

Figure 7. a) Schematic illustration for the all-solid-state zinc-air battery. b) Photograph of a lighted LED powered by two all-solid-state Zn-air batteries. c) Mechanical flexibility test of the solid-state rechargeable Zn-air battery between flat and fold states for each 10 cycles.

atmosphere for 2 h and the obtained catalysts were denoted as NPC-800, NPC-900 and NPC-1000, respectively.

Materials characterization: The field emission scanning electron microscopy (FESEM; Zeiss, Sigma 300) and transmission electron microscopy (JEOL 2100 PLUS) were performed to characterize the morphologies of the carbon materials. The high-resolution TEM (HRTEM) images and elemental mappings were obtained using FEI TF20. The crystalline structure was characterized through X-ray diffractometer Bruker D8 with Cu Kα radiation (I = 0.15418 nm). The surface composition of samples was determined through the X-ray photoelectron spectroscopy (XPS) of Thermo ESCALAB 250xl. The Raman spectroscopy was analysed by Raman spectra on LabRAM HR800 (HORLBA JY). The specific surface area and pore size distribution were obtained through nitrogen sorption measurements (Kubo-x1000).

Electrochemical characterization: A three-electrode system was used to measure the electrochemical properties on an electrochemical workstation (CHI760E). The counter electrode and the reference electrode were platinum sheet and Ag/AgCl. All potentials measured were calibrated to the RHE using the following equation: $E\ (RHE) = E^{\ominus}\ (Ag/AgCl) + 0.059pH$. The sample ink was prepared by dispersing 6 mg of NPC catalysts in ethanol (300 μL) and DI water (900 μL) under ultrasonication. Then, 10 μL sample ink was loaded onto the working electrode with 0.5% Nafion as the binder to achieve a mass loading of 200 μg cm⁻² on the basis of the geometric area of the disc electrode. The electrochemical properties of electrocatalysts for ORR and OER were characterized through linear sweep voltammetry (LSV) measurements were implemented at a scan rate of 5 mV s⁻¹, cyclic voltammetry (CV), electrochemical impedance spectroscopy (EIS) and amperometric i–t curve.

The assembly of Zn-air battery: The carbon cloth was washed and then used as the support for loading catalysts (1 mg cm⁻²). A gel polymer electrolyte was prepared by utilizing N,N′-methylenebisacrylamide (MBA) as the cross-linking agent, acrylic acid as the monomer and $K_2S_2O_4$ as the initiator. All measurements were carried out on a LAND battery testing system (CT2001A).

Acknowledgements

Conflict of Interest

The authors declare no conflict of interest.

Keywords: bifunctional electrocatalysis · flexible batteries · nitrogen-doped porous carbon · solid-state batteries · Zinc-air batteries

[1] a) Z. W. Seh, J. Kibsgaard, C. F. Dickens, I. Chorkendorff, J. K. Nørskov, T. F. Jaramillo, *Science* **2017**, *355*, eaad4998; b) J. L. Liu, D. D. Zhu, C. X. Guo, A. Vasileff, S. Z. Qiao, *Adv. Energy Mater.* **2017**, 1700518.

[2] a) J. S. Lee, S. T. Kim, R. G. Cao, N. S. Choi, M. L. Liu, K. T. Lee, J. Cho, *Adv. Energy Mater.* **2011**, *1*, 34–50; b) Y. Y. Huang, Y. Q. Wang, C. Tang, J. Wang, Q. Zhang, Y. B. Wang, J. T. Zhang, *Adv. Mater.* **2018**, 1803800.

[3] J. Pan, Y. Y. Xu, H. Yang, Z. H. Dong, H. F. Liu, B. Y. Xia, *Adv. Sci.* **2018**, 1700691.

[4] a) L. M. Dai, Y. H. Xue, L. Y. Qu, H. J. Choi, J. Baek, *Chem. Rev.* **2015**, *115*, 4823–4892; b) M. G. Wu, Y. Q. Wang, Z. X. Wei, L. Wang, M. Zhuo, J. T. Zhang, X. P. Han, J. M. Ma, *J. Mater. Chem. A* **2018**, *6*, 10918–10925.

[5] a) L. Z. Bu, N. Zhang, S. J. Guo, X. Zhang, J. Li, J. L. Yao, T. Wu, G. Lu, J. Y. Ma, D. Su, X. Q. Huang, *Science* **2016**, *354*, 1410–1414; b) H. J. Guo, X. Zhang, J. G. X. Zhu, G. Lu, X. Q. Huang, *Sci. Adv.* **2017**, *3*, e1601705.

[6] L. C. Seitz, C. F. Dickens, K. Nishio, Y. Hikita, J. Montoya, A. Doyle, C. Kirk, A. Vojvodic, H. Y. Hwang, J. K. Norskov, T. F. Jaramillo, *Science* **2016**, *353*, 1011–1034.

[7] D. F. Yan, Y. X. Li, J. Huo, R. Chen, L. M. Dai, S. Y. Wang, *Adv. Mater.* **2017**, *29*, 1606459.

[8] J. T. Zhang, H. L. Li, P. Z. Guo, H. Y. Ma, X. S. Zhao, *J. Mater. Chem. A* **2016**, *4*, 8497–8511.

[9] a) Z. F. Huang, J. Wang, Y. C. Peng, C. Y. Jung, A. Fisher, X. Wang, *Adv. Energy Mater.* **2017**, *7*, 1700544; b) L. Wang, Y. Q. Wang, M. G. Wu, Z. X. Wei, C. Y. Cui, M. L. Mao, J. T. Zhang, X. P. Han, Q. H. Liu, J. M. Ma, *Small* **2018**, *14*, e1800737.

[10] J. T. Zhang, L. M. Dai, *ACS Catal.* **2015**, *5*, 7244–7253.

[11] K. P. Gong, F. Du, Z. H. Xia, M. Durstock, L. M. Dai, *Science* **2009**, *323*, 760–764.

[12] a) J. T. Zhang, Z. H. Xia, L. M. Dai, *Sci. Adv.* **2015**, *1*, e1500564; b) Q. Lv, W. Y. Si, Z. Yang, N. Wang, Z. Y. Tu, Y. P. Yi, C. S. Huang, L. Jiang, M. J. Zhang, J. J. He, Y. Z. Long, *ACS Appl. Mater. Interfaces* **2017**, *9*, 29744–29752.

[13] L. T. Qu, Y. Liu, J. B. Baek, L. M. Dai, *ACS Nano* **2010**, *4*, 1321–1326.

[14] D. h. Guo, R. Shibuya, C. Akiba, S. Saji, T. Kondo, J. Nakamura, *Science* **2016**, *351*, 361–365.

[15] C. Z. Zhu, S. F. Fu, B. Z. Xu, J. H. Song, Q. R. Shi, M. H. Engelhard, X. L. Li, S. P. Beckman, J. M. Sun, D. Du, Y. H. Lin, *Small* **2017**, *13*, 1700796.

[16] B. H. R. Suryanto, S. Chen, J. J. Duan, C. Zhao, *ACS Appl. Mater. Interfaces* **2016**, *8*, 35513–35522.

[17] J. T. Zhang, L. T. Qu, G. Q. Shi, J. Y. Liu, J. F. Chen, L. M. Dai, *Angew. Chem. Int. Ed.* **2016**, *55*, 2230–2234; *Angew. Chem.* **2016**, *128*, 2270–2274.

[18] J. T. Zhang, Z. H. Zhao, Z. H. Xia, L. M. Dai, *Nat. Nanotechnol.* **2015**, *10*, 444–452.

[19] W. Y. Zhang, X. C. Xu, C. X. Zhang, Z. H. Yu, Y. M. Zhou, Y. W. Tang, P. Wu, S. J. Guo, *Small Methods* **2017**, *1*, 1700167.

[20] X. C. Gao, L. W. Wang, J. Z. Ma, Y. Q. Wang, J. T. Zhang, *Inorg. Chem. Front.* **2017**, *4*, 1582–1590.

[21] L. L. Zhang, A. Q. Wang, W. T. Wang, Y. Q. Huang, X. Y. Liu, S. Miao, J. Y. Liu, T. Zhang, *ACS Catal.* **2015**, *5*, 6563–6572.

[22] L. F. Lai, J. Potts R., D. Zhan, L. Wang, C. K. Poh, C. H. Tang, H. Gong, Z. X. Shen, J. Y. Lin, R. S. Ruoff, *Energy Environ. Sci.* **2012**, *5*, 7936–7942.

[23] C. Tang, H. F. Wang, X. Chen, B. Q. Li, T. Z. Hou, B. S. Zhang, Q. Zhang, M. M. Titirici, F. Wei, *Adv. Mater.* **2016**, *28*, 6845–6851.

[24] B. He, F. J. Liu, S. K. Yan, *J. Mater. Chem. A* **2017**, *5*, 18064–18070.

[25] C. Tang, Q. Zhang, *Adv. Mater.* **2017**, *29*, 1604103.

[26] Y. Tong, P. Z. Chen, T. P. Zhou, K. Xu, W. S. Chu, C. Z. Wu, Y. Xie, *Angew. Chem. Int. Ed.* **2017**, *56*, 7121–7125; *Angew. Chem.* **2017**, *129*, 7227–7231.

[27] Q. Liu, Y. B. Wang, L. M. Dai, J. N. Yao, *Adv. Mater.* **2016**, *28*, 3000–3006.

[28] J. Zhang, H. Zhou, J. W. Zhu, P. Hu, C. Hang, J. L. Yang, T. Peng, S. C. Mu, Y. H. Huang, *ACS Appl. Mater. Interfaces* **2017**, *9*, 24545–24554.

[29] a) L. S. Amiinu, Z. H. Pu, X. B. Liu, K. A. Owusu, H. G. R. Monestel, F. O. Boakye, H. N. Zhang, S. C. Mu, *Adv. Funct. Mater.* **2017**, *27*, 1702300; b) Z. H. Wang, H. H. Jin, T. Meng, K. Liao, W. Q. Meng, J. L. Yang, D. P. He, Y. L. Xiong, S. C. Mu, *Adv. Funct. Mater.* **2018**, *28*, 1802596; c) D. Bin, B. Yang, C. Li, Y. Liu, X. Zhang, Y. Wang, Y. Xia, *ACS Appl. Mater. Interfaces* **2018**, *10*, 26178–26187.

[30] W. L. Zhang, C. Xu, C. Q. Ma, G. X. Li, Y. Z. Wang, K. Y. Zhang, F. Li, C. Liu, H. M. Cheng, Y. W. Du, N. J. Tang, W. C. Ren, *Adv. Mater.* **2017**, *29*, 1701677.

[31] Y. Y. Guo, P. F. Yuan, J. N. Zhang, Y. F. Hu, I. S. Amiinu, X. Wang, J. G. Zhou, H. C. Xia, Z. B. Song, Q. Xu, S. C. Mu, *ACS Nano* **2018**, *12*, 1894–1901.

[32] M. L. Zhang, Y. G. Wang, W. X. Chen, J. C. Dong, L. R. Zheng, J. Luo, J. W. Wan, S. B. Tian, W. C. Cheong, D. S. Wang, Y. D. Li, *J. Am. Chem. Soc.* **2017**, *139*, 10976–10979.

[33] G. T. Fu, Y. F. Chen, Z. M. Cui, Y. T. Li, W. D. Zhou, S. Xin, Y. W. Tang, J. B. Goodenough, *Nano Lett.* **2016**, *16*, 6516–6522.

[34] C. Guan, A. Sumboja, H. Wu, W. Ren, X. Liu, H. Zhang, Z. Liu, C. Cheng, S. J. Pennycook, J. Wang, *Adv. Mater.* **2017**, *29*.

[35] M. S. Balogun, W. T. Qiu, Y. C. Huang, H. Yang, R. M. Xu, W. X. Zhao, G. R. Li, H. B. Ji, Y. X. Tong, *Adv. Mater.* **2017**, *29*, 1702095.

[36] H. W. Liang, X. D. Zhuang, S. Bruller, X. L. Feng, K. Mullen, *Nat. Commun.* **2014**, *5*, 4973.

[37] I. S. Amiinu, Z. H. Pu, X. B. Liu, K. A. Owusu, H. G. R. Monestel, F. O. Boakye, H. N. Zhang, S. C. Mu, *Adv. Funct. Mater.* **2017**, *27*, 1702300.

[38] L. Qin, L. Wang, X. Yang, R. Ding, Z. Zheng, X. Chen, B. Lv, *J. Catal.* **2018**, *359*, 242–250.

[39] H.-F. Wang, C. Tang, B. Wang, B.-Q. Li, X. Cui, Q. Zhang, *Energy Storage Mater.* **2018**, *15*, 124–130.

[40] C. Lin, S. S. Shinde, Y. Wang, Y. Sun, S. Chen, H. Zhang, X. Li, J.-H. Lee, *Sustain. Energy Fuels* **2017**, *1*, 1909–1914.

[41] S. Peng, X. Han, L. Li, S. Chou, D. Ji, H. Huang, Y. Du, J. Liu, S. Ramakrishna, *Adv. Energy Mater.* **2018**, *8*, 1800612.